RESEARCH ARTICLE

NMR IN BIOMEDICINE WILEY

Quantitative platform for accurate and reproducible assessment of transverse (T_2) relaxation time

Dvir Radunsky[1] | Neta Stern[1] | Jannette Nassar[1] | Galia Tsarfaty[2] |
Tamar Blumenfeld-Katzir[1] | Noam Ben-Eliezer[1,3,4]

[1]Department of Biomedical Engineering, Tel Aviv University, Israel

[2]Department of Diagnostic Imaging, Sheba Medical Center, Ramat Gan, Israel

[3]Sagol School of Neuroscience, Tel Aviv University, Israel

[4]Center for Advanced Imaging Innovation and Research (CAI2R), New York University Langone Medical Center, New York, New York, USA

Correspondence
Dr Noam Ben-Eliezer, Department of Biomedical Engineering, Tel Aviv University, Tel Aviv 6997801, Israel.
Email: noambe@tauex.tau.ac.il

MRI's transverse relaxation time (T_2) is sensitive to tissues' composition and pathological state. While variations in T_2 values can be used as clinical biomarkers, it is challenging to quantify this parameter in vivo due to the complexity of the MRI signal model, differences in protocol implementations, and hardware imperfections. Herein, we provide a detailed analysis of the echo modulation curve (EMC) platform, offering accurate and reproducible mapping of T_2 values, from 2D multi-slice multi-echo spin-echo (MESE) protocols.

Computer simulations of the full Bloch equations are used to generate an advanced signal model, which accounts for stimulated echoes and transmit field (B_1^+) inhomogeneities. In addition to quantifying T_2 values, the EMC platform also provides proton density (PD) maps, and fat-water fraction maps. The algorithm's accuracy, reproducibility, and insensitivity to T_1 values are validated on a phantom constructed by the National Institute of Standards and Technology and on in vivo human brains.

EMC-derived T_2 maps show excellent agreement with ground truth values for both in vitro and in vivo models. Quantitative values are accurate and stable across scan settings and for the physiological range of T_2 values, while showing robustness to main field (B_0) inhomogeneities, to variations in T_1 relaxation time, and to magnetization transfer. Extension of the algorithm to two-component fitting yields accurate fat and water T_2 maps along with their relative fractions, similar to a reference three-point Dixon technique.

Overall, the EMC platform allows to generate accurate and stable T_2 maps, with a full brain coverage using a standard MESE protocol and at feasible scan times. The utility of EMC-based T_2 maps was demonstrated on several clinical applications, showing robustness to variations in other magnetic properties. The algorithm is available online as a full stand-alone package, including an intuitive graphical user interface.

KEYWORDS
clinical biomarker, quantitative MRI, T_2 accuracy, T_2 mapping, T_2 relaxation

---

1 | INTRODUCTION

MRI technology is one of the most advanced and safest ways of investigating anatomy and physiology processes in vivo. The use of contrast-weighted images in clinical routine produces fundamentally qualitative data, which may lead to observer-dependent radiologic interpretation. To address this problem, the field of MRI is gradually adopting a more objective data representation termed quantitative MRI (qMRI). Quantitative scans allow us to expand the dynamic range of MRI's contrast mechanisms and produce numeric values (eg diffusion coefficient or relaxation time constants) that can be used as clinical biomarkers.[1–3] Thus, qMRI techniques that produce accurate and reproducible quantitative data can improve the discernibility of anatomical and physiological changes, and allow easier follow-up of the patient's status over time.

MRI's transverse relaxation time (ie T_2) is one of the central contrast mechanisms being used to investigate pathologies including stroke, multiple sclerosis (MS), cardiac disease, cancer lesions (eg prostate carcinoma), musculoskeletal diseases, and dysregulated iron content.[4–7] Notwithstanding the significant investment in developing quantitative T_2 (qT_2) mapping techniques, the dissemination of qT_2 is still hindered by the lack of a gold standard that can provide accurate and reproducible values across scanners and scan settings. It is important to note that changes in the tissue composition might alter several relaxation times simultaneously; eg, both T_2 and T_2^* are affected by the iron depositions in the liver.[8]

To map T_2 values in vivo one would typically use a 2D multi-slice multi-echo spin-echo (MESE) protocol, which offers the highest sensitivity to this relaxation time at scan times of about 5 min (depending on the matrix size and coverage). The use of this protocol, however, raises a serious difficulty as its signal decay curve strongly deviates from a theoretical exponential model due to the presence of stimulated and indirect echoes,[9] leading to a significant overestimation of T_2 values.[10] This bias is, moreover, not constant and varies between protocol implementations and scan parameters such as the pulse-sequence timing diagram, RF pulse shapes, refocusing flip angle (FA), echo time (TE), slice thickness, acquisition bandwidth (BW), and B_1^+ profile.[11–14] These influence the signal decay pattern, and must therefore be incorporated into the data processing procedures in order to generate reproducible T_2 values.

Advanced qT_2 techniques attempt to compensate for the MESE signal deviations either by excluding some of the data points to mimic a more exponential decay pattern,[15] by modelling the effects of stimulated echoes, eg the extended phase graph (EPG) formalism[10] and echo compensation,[16,17] or by using non-MESE acquisition schemes, eg MRF[18] and mcDESPOT.[19] Another approach that uses the MESE protocol, yet avoids the need for tracking the myriad of coherence pathways[10] (see Supplementary Figure S1), is to simulate the evolution of the spin system using the time-dependent Bloch equations. This approach is employed by the echo modulation curve (EMC) algorithm, which simulates the spin dynamics during MESE acquisitions, while accounting for the particular pulse sequence timing diagram (eg RF pulses, gradient events, and B_1^+ inhomogeneity[20]). This results in a faithful representation of the signal, and highly accurate T_2 values that closely match the values obtained using reference single spin-echo (SSE) and spectroscopic acquisitions. Tailoring the fitting procedures to the specific scan settings provides further stability across protocol implementations, scanners, and scan parameters.[20,21] By delivering the true T_2 values of tissues the EMC algorithm allows the quantification of secondary spin dynamic mechanisms, such as magnetization transfer (MT) and diffusion,[22,23] providing further insight into the tissues' state.

The idea of Bloch-based mapping of T_2 values was introduced in previous work.[20] Herein we provide a comprehensive review of this approach, while covering new and important aspects of the EMC platform including validation experiments, regularization of the B_1^+ spatial profile, T_1 insensitivity, fat-water fraction analysis, the clinically oriented user interface, and data denoising. We further include theoretical and practical aspects of the core fitting algorithm, detailed analysis of the method's limitations, and effects of MT, and present examples of its clinical applicability.

2 | METHODS

2.1 | Non-exponential decay pattern of MESE signals

MESE protocols employ trains of slice-selective RF pulses, which lead to an unavoidable contamination of the measured signal by stimulated and indirect echoes. These arise due to the inherently non-rectangular slice profile of the refocusing RF pulses, causing each pulse to impart a range of FAs, from zero to $180°$ and back to zero, instead of a flat $180°$ refocusing.[12] Thus, each RF splits the signal into three coherence pathways[10]: a full $180°$ inversion, a $90°$ FA, and a third pathway, which is unaffected by the RF pulse (for more details see Supplementary Figure S1). The number of coherence pathways continues to grow exponentially, and eventually reaches 3^{ETL}, where ETL is the echo train length (and the number of refocusing RF pulses). Only a subset of these coherence pathways is "visible" during the formation of each spin-echo, causing MESE signals to significantly deviate from the theoretical exponential decay pattern.

2.2 | The core EMC algorithm

Figure 1 presents a flowchart of the core EMC algorithm, consisting of three main stages.

Stage I, Data acquisition

Stage III, Postprocessing:
The generation of T₂ and PD maps

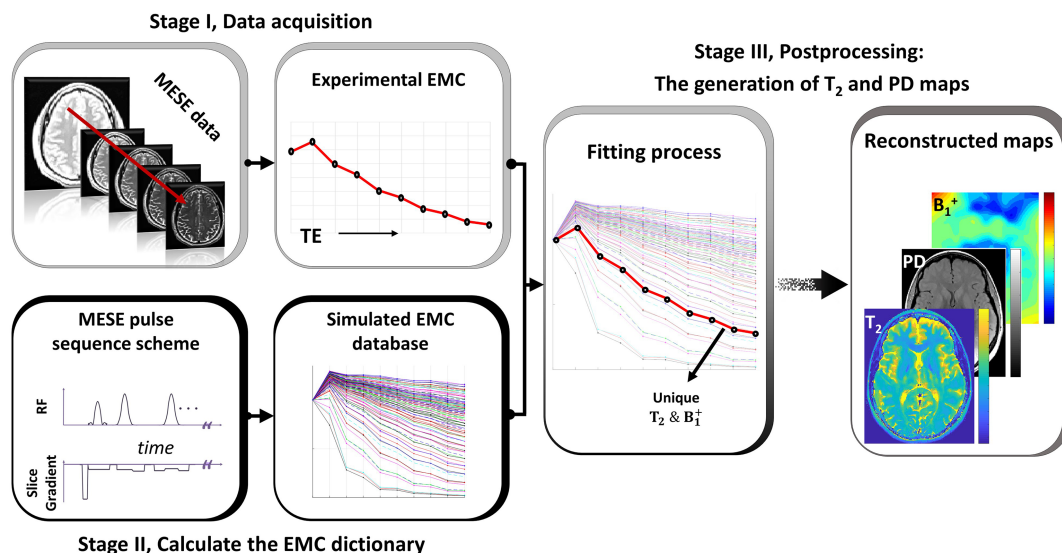**Stage II, Calculate the EMC dictionary**

FIGURE 1 Flowchart of the EMC algorithm, consisting of three main stages: Stage I, data acquisition using 2D multi-slice MESE protocol, producing an *experimental EMC* per voxel; Stage II, simulations of the EMC dictionary for a range of T_2 and B_1^+ values, producing a dictionary of *simulated EMCs*; Stage III, voxel-by-voxel fitting, where each *experimental EMC* is matched to the series of *simulated EMCs* by computing the minimal L^2 norm of the difference between the two, resulting in qT_2 and B_1^+ maps. Finally, a PD map is reconstructed based on the calculated T_2 map and the first echo image (see text for more details)

Stage 1. *Data acquisition*. Experimental 2D MESE data are acquired for a set of gradually increasing *T*E values, producing a series of T_2-weighted images. We denote the time-dependent signal at each voxel as EMC^{experimental}.

Stage 2. *Preprocessing—calculation of an EMC dictionary*. Bloch simulations are used to calculate the theoretical signal decay curve that is expected to arise from an experimental MESE protocol. The RF pulse shape and duration are imported from the scanner and incorporated into the simulation, accounting also for T_1 and T_2 relaxation during the application of the RF pulses. Each simulation cycle generates a single EMC^{simulated}, predicting the signal intensity for a specific T_2 relaxation time and B_1^+ inhomogeneity level. A full dictionary of simulated EMCs is assembled by repeating the simulations, each time with a different T_2 value (1, ..., 1000 ms) and B_1^+ inhomogeneity scale (80%, ..., 120%), where 100% corresponds to a perfectly homogeneous field. Finally, the simulated EMCs are normalized to the first echo intensity, factoring out the dependence on local proton density (PD) and receive coil profile (B_1^-). A key aspect of the dictionary generation process is that it simulates the spin dynamics only along the slice dimension (z, t), rather than the full 4D space (x, y, z, t). This simplification reduces the computational time significantly, and is justified by the fact that it is only the imperfect slice profile that is actually responsible for the emergence of stimulated echoes. We note that simulations do not account for spoiling between repetition times, but assume that the magnetization is in steady state owing to the use of relatively long *T*R (3 s and above).

Stage 3. *Postprocessing—generation of T_2 and PD maps*. To improve data reliability, we start this stage by removing low SNR time points from each experimental EMC. Rician noise will bias magnitude images when the signal intensity is low[24] (ie where SNR < 2-3), leading to reduced fitting accuracy. To avoid this, we truncate the signal time-series when its intensity decreases below 10% of the first echo. Fitting is then done by matching the experimental signal from each voxel (EMC^{experimental}, from Stage 1) to the dictionary of simulated EMCs (EMC^{simulated}, from Stage 2), and choosing the dictionary entry with the lowest L^2 norm difference between the two EMCs:

$$\min_{T_2, B_1^+} \left\| EMC^{experimental} - EMC^{simulated}\left(T_2, B_1^+\right) \right\|_2^2. \tag{1}$$

A unique pair of T_2 and B_1^+ values is thus assigned to each voxel, generating the full parametric map. Finally, PD maps are calculated by back-projecting the intensity of each voxel in the first *T*E image to time $t = 0$ using its calculated T_2 value. A pure exponential decay takes place between the excitation and the first echo formation, as no stimulated echoes appear before the second echo is acquired.

A key aspect of the spin temporal evolution is that it will vary between different protocol implementations and scan parameters. Tailoring the reconstruction process to the specific pulse sequence scheme and scan parameters is thus an essential part of standardizing qMRI, and critical for

producing reproducible T_2 values. Cross-vendor stability is particularly important, as each vendor has its own specific protocol implementations, causing MESE decay patterns to vary between scanners and different main magnetic fields (see Supplementary Figure S2).

2.3 | Compensating for B_1^+ inhomogeneities

The extensive use of RF pulses in MESE protocols causes the experimental EMC signal to be dependent on the B_1^+ field profile. To avoid bias of the fitted T_2 maps due to inhomogeneities of the B_1^+ field, the EMC dictionary holds a second dimension, corresponding to different B_1^+ values. The fitting process thus produces a second parametric map describing the B_1^+ inhomogeneity profile. Straightforward voxel-by-voxel fitting is not sufficient in this case, as some ambiguities might arise due to noise potentially causing more than one $[T_2, B_1^+]$ dictionary entry to match the same experimental curve. To address this problem, we incorporated into the fitting process a constraint, imposing spatial smoothness of the B_1^+ field. This is implemented by running the dictionary matching process twice. The first iteration produces the initial T_2 and B_1^+ maps, using no a priori knowledge. The resulting B_1^+ values are then filtered, extracting from the B_1^+ map outlier values based on Chauvenet's criterion[25] (with two standard deviations), and factoring out potential fitting errors in areas of extremely short/long T_2 values (ie, T_2 < echo spacing (esp) or T_2 > 2 x esp x ETL, respectively). The missing B_1^+ values are then filled by interpolating the remaining values over the entire field of view, and smoothed using a 15×15 voxel window. The resulting map is finally inputted to a second fitting iteration, in which the possible B_1^+ range is limited to the input map ± 3%.

2.4 | Validation experiments

Accuracy, reproducibility and repeatability scores were evaluated using the National Institute of Standards and Technology (NIST) phantom[26] (Model 130-0049) and in vivo human brain. All scans were performed on a whole-body 3 T scanner (Siemens Prisma) and a 20-channel receiver coil using standard SSE and MESE protocols. In vivo data were collected from five healthy volunteers (29 ± 4 years old, three females), after obtaining informed consent and under the approval of our IRB committees.

Reference objects, such as chemical solution phantoms, can be used to mimic tissue properties and help facilitate standardization in the qMRI field. The T_2 array of the NIST phantom contains water doped with different concentrations of $MnCl_2$, generating a T_2 range of approximately 5-600 ms. The results presented here include sphere numbers 4-12, matching a typical physiological range of $T_2 = 11$ to 185 ms. The EMC mapping *accuracy* was evaluated as the relative error between SSE- and MESE-derived T_2 values, and presented on a Bland-Altman plot for agreement between the protocols. Scan parameters were the following: $TR = 6000$ ms (SSE), 3000 ms (MESE); esp = 10 ms; $N_{Echoes} = 1$ (SSE), 25 (MESE); resolution = $1.0 \times 1.0 \times 4.0$ mm^3; BW = 200 Hz/Px; $N_{slices} = 1$; acceleration = ×2 GRAPPA (MESE); refocusing FA = 180°; $T_{acq} = 3$ h 5 min 10 s (SSE), 4 min 38 s (MESE); $N_{Avg.} = 2$. T_2 maps were generated using mono-exponential fitting of the SSE data, and using the EMC algorithm for the MESE data.[20] Mean T_2 ± SD values were calculated for each sphere.

Test-retest reliability was evaluated by repeating the MESE scan 15 times, and measuring the SD across scans. The *reproducibility* of EMC-derived values was evaluated by repeating the MESE scans with different scan settings, and comparing the results with the reference values from the accuracy experiment described above. The scan parameters tested were the following: pixel size = 1.0×1.0, 1.6×1.6 mm^2; BW = 200, 300, 401 Hz/Px; slice thickness = 3, 4, 5 mm; $N_{slices} = 1, 3, 5, 9, 11$ (inter-slice gap = 0%); inter-slice gap = 0, 50, 100, 200% ($N_{slices} = 5$); TR = 2, 3, 4 s; FA = 180°, 160°, 140°.

The fitting accuracy and reproducibility of the EMC algorithm were also investigated in vivo, on five human brains, by comparing the T_2 values in a series of manually segmented regions of interest (ROIs), each covering an area of 4×4 voxels. ROIs were positioned in the parietal bone, genu of the corpus callosum (CC), frontal lobe's white matter (WM) fascicles, thalamus, and insular gray matter (GM). Accuracy measurements were applied between reference SSE data processed using exponential fitting, and MESE data, reconstructed using the EMC algorithm. The protocols employed seven TE values = 15:15:105 ms, with a total scan time of 3 min 2 s and 21 min 14 s for the MESE and SSE respectively. Scan parameters were the following: $TR/TE = 2000/15$ ms; resolution = $1.0 \times 1.0 \times 3.0$ mm^3; BW = 200 Hz/Px; $N_{slices} = 8$; acceleration = ×2 GRAPPA; refocusing FA = 180°. Reproducibility measurements were performed for the MESE-derived T_2 maps, using different scan settings: BW = 200, 303 Hz/Px; slice thickness = 2, 3 mm; TR = 2, 3 s; FA = 180°, 150°. For both accuracy and reproducibility measurements, the mean and SD T_2 values were calculated in each ROI, and were also averaged across volunteers to evaluate inter-subject variability.

2.5 | Preprocessing denoising of MESE images

To improve fitting precision, we applied image denoising to the in vivo data. Denoising was done using the Marchenko-Pastur principal component analysis algorithm[27] implemented for MESE data, using a sliding window of size ETL $\times 5 \times 5$. This algorithm is aimed at removing thermal

noise, and may not be effective for removing signal contamination by other artifacts. To keep a fair comparison between MESE and SSE values we also applied the same preprocessing procedure on the SSE data by combining the set of separate SSE images from each TE to a single time-series before denoising.

2.6 | Effect of T_1 relaxation on qT$_2$ values

Clinical MESE acquisitions are significantly shorter compared with the voxel-average T_1 relaxation times, which are, in turn, shorter than the typical TR (ie, esp $\times$ ETL $\ll T_1 < TR$). As a result, MESE protocols have poor sensitivity to T_1, making the resulting T_2 maps impervious to variations in the images' T_1 weighting. These can occur when using different TR values, as the T_1 relaxation simply attenuates the signal baseline without affecting the T_2 decay pattern. As a result, T_1 has a negligible effect on the quantitative estimation of T_2. To further validate this hypothesis, we generated 16 simulated EMCs, where each curve holds a unique pair of $[T_1, T_2]$ values and examined the effect of different T_1 values on a specific T_2 value. This test was repeated for two physiological regimes of T_1/T_2 ratios[28–31]: short T_2 values of 15-20 ms with $T_1 = 0.2:0.1:0.5$ s, and mid-range T_2 values of 50-60 ms with $T_1 = 0.65:0.45:2$ s.

2.7 | Estimation of fat-water fraction

An extension of the EMC algorithm for two T_2 component fitting was recently presented by Nassar et al.[32] By separating the different contributions of the fat and water T_2 components, the technique allows to quantify the relative fat and water fractions in each voxel. Herein, we demonstrate this ability by calculating the fat-water fractions of diseased thigh muscle, reconstructed using the EMC platform and using the three-point Dixon technique.[33] Data were collected on a single patient (male, 36 years old) with a genetically confirmed dysferlinopathy, recruited and scanned at the Centre de Résonance Magnétique Biologique et Médicale (CRMBM) in Marseille, France. Patients' scans were held done on a 1.5 T Siemens scanner (Avanto) using an eight-channel flexible matrix coil, and the protocol was approved by the local ethics committee (Comité de Protection des Personnes Sud Méditerranée I). Fat-water maps were automatically segmented using a deep learning neural network to exclude the subcutaneous fat and fibula and tibia bones.[34] Two quantitative biomarkers were computed based on the maps: Biomarker 1 (*viable muscle fraction*), the fraction of viable tissue out of the entire muscle (ie where fat fraction is <50%), and Biomarker 2 (*fat infiltration index*), the mean fat fraction within the viable muscle region. MESE scan parameters were the following: $TR/TE = 1479/8.7$ ms; $N_{\text{Echoes}} = 17$, resolution $= 1.5 \times 1.5 \times 10.0$ mm^3; acceleration $= \times 2$ GRAPPA; $T_{\text{acq}} = 5$ min 7 s.

3 | RESULTS

3.1 | Example: EMC-based quantitative maps

Figure 2 presents a series of qT$_2$ and PD maps, alongside T_2-weighted images, for three models—in vivo brain, in vivo calf, and the NIST phantom. The calf PD map is also weighted by the receiver coil sensitivity profile, exemplifying one of the general limitations of mapping tissues' PD.

Figure 3 illustrates an EMC-based B_1^+ map for a water phantom doped with MnCl$_2$, having a uniform T_2 of 92 ms. The uniformity of this phantom allows to isolate the hardware-induced B_1^+ transmit profile, independent of structural influences. As can be seen, the natural field's inhomogeneity has a radial distribution pattern, decreasing from the scanner's isocenter towards its periphery. Such B_1^+ profile maps are incorporated by the EMC fitting procedure to achieve higher accuracy of T_2 values.

The EMC platform is readily available via a simple and easy to use GUI (see Supplementary Figure S3); the code package is accessible at https://beneliezer-lab.com/software-downloads-page/.

3.2 | Validation experiments

The EMC accuracy and reproducibility are illustrated in Table 1 and Figures 4 and 5 for the T_2 array of the NIST phantom. Table 1 exemplifies the high accuracy of the EMC-derived T_2 values, which are in strong agreement with reference SSE values. Even more prominent is the higher precision achieved by the MESE protocol and reflected by the consistently lower spread of T_2 values (ie smaller SD), attesting to the EMC algorithm's robustness to thermal and reconstruction noise. The average relative error between the two protocols was found to be 0.4 ± 2.9%. While a small change of 0.4% reflects the high accuracy of EMC-derived T_2 values, both negative and positive errors were observed across the different spheres. The average absolute differences between the measured and the reported values by NIST were 4.7% and 3.7% for SSE and MESE
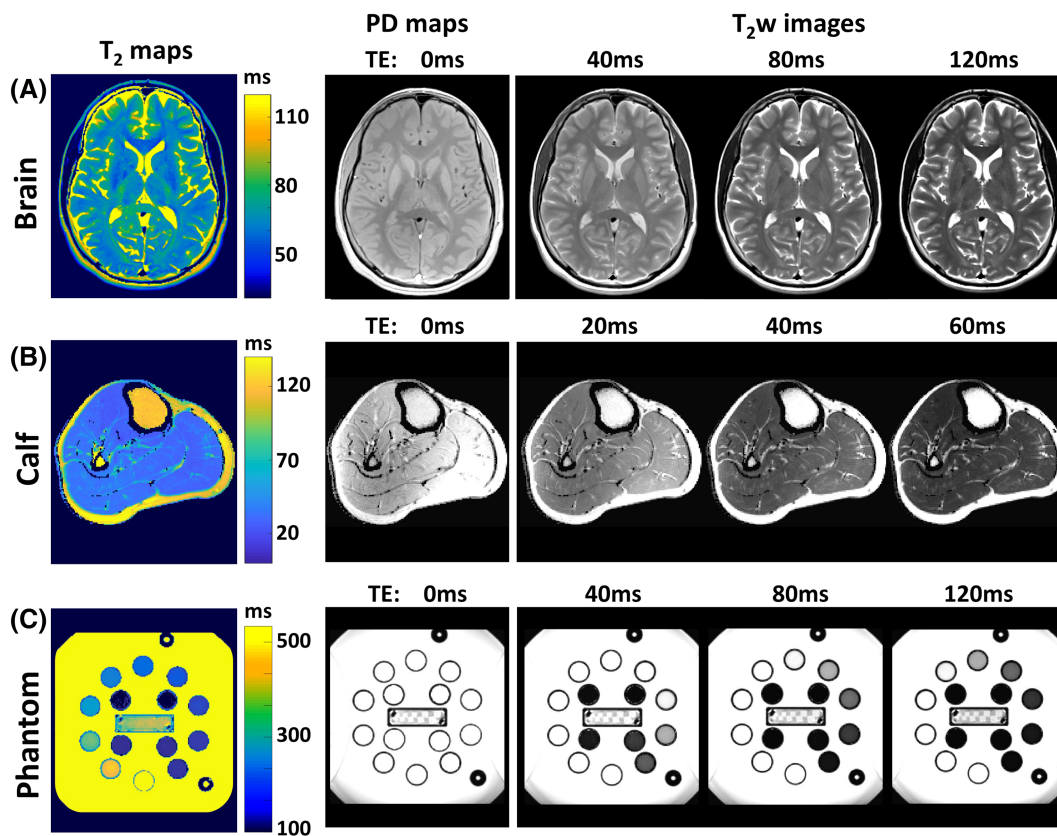
FIGURE 2 qT$_2$ maps and T_2-weighted images at arbitrary TE values (ms), generated using the EMC algorithm for in vivo brain (A), in vivo calf (B), and the T_2 array of the NIST phantom (C). Scan parameters: TR/TE = 3000/10 ms; N_{Echoes} = 30, resolution = 1.5 × 1.5 × 3.0 (brain), 0.8 × 0.8 × 5.0 (calf), 1.0 × 1.0 × 4.0 (phantom) mm^3; BW = 200 Hz/Px; N_{slices} = 1; acceleration = 2× GRAPPA; T_{acq} = 3 min 17 s (brain), 4 min 26 s (calf), 4 min 38 s (phantom); $N_{Avg.}$ = 2 (phantom only)
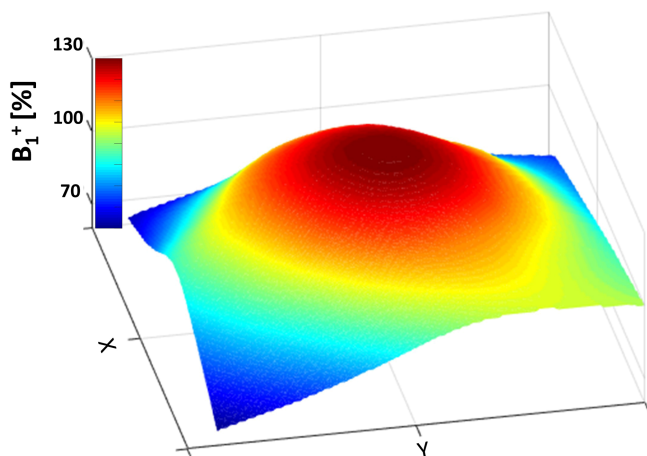

FIGURE 3 EMC-fitted B_1^+ inhomogeneity map for a uniform phantom of water doped with MnCl$_2$. The homogeneity of the transmit field is presented as a percentage, where 100% represents no bias. The phantom was scanned on a whole-body 3 T scanner (Siemens Prisma) using a standard MESE protocol. Scan parameters: TR/TE = 6000/10 ms; N_{Echoes} = 30; BW = 200 Hz/Px; resolution = 1.0 × 1.0 × 4.0 mm^3

respectively. This suggests that EMC-derived values might be even more accurate than the reference SSE, possibly due to diffusion bias of SSE values. The average coefficient of variation (CV) reflects the method's stability, and was found to be 6.8% for SSE-derived T_2 values, and 2.5% for MESE. It is important to mention that the actual T_2 values of our phantom might be slightly different from the ones reported by NIST, as the scans were performed two years after purchasing this phantom.

Figure 4 shows correlation and Bland-Altman plots of agreements between SSE and MESE-derived T_2 values, comparing the values per voxel in all nine spheres (total of 423 voxels). The EMC-derived qT$_2$ values were scattered as a function of the SSE reference values, revealing a clear linear relation between the two methods, with an R^2 score of 0.996 (Figure 4A). T_2 difference was plotted as a function of the average T_2 in each voxel, yielding a mean difference of 1.6 ± 4.7 ms (Figure 4B). For a confidence level of 95%, the limits of agreement are [−7.7, 10.9] ms, which

TABLE 1 qT_2 values for the NIST phantom (T_2 array) calculated from SSE and MESE data. Mean T_2 and SD values were estimated for circular ROIs within the spheres (see Figure S4), containing 47 voxels each. The relative difference between the two protocols (%) was calculated according to $100 \times (T_{2,MESE} - T_{2,SSE})/T_{2,SSE}$

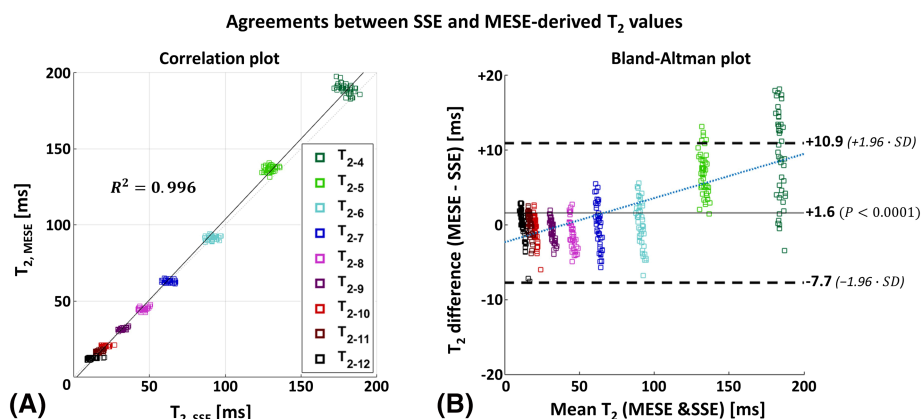| Sphere no	Reported T_2 (ms)	SSE T_2 (ms)	SD (ms)	CV (%)	MESE T_2 (ms)	SD (ms)	CV (%)	Diff. vs SSE (ms)
T_2-4	184.8	179.3	4.0	2	189.0	3.2	2	5.4
T_2-5	134.1	129.7	2.7	2	136.6	1.8	1	5.3
T_2-6	94.4	90.9	2.9	3	91.2	1.3	1	0.3
T_2-7	62.5	63.2	2.6	4	62.8	0.9	1	−0.6
T_2-8	45.0	45.9	2.2	5	44.8	1.0	2	−2.4
T_2-9	31.0	32.1	1.9	6	31.6	0.7	2	−1.6
T_2-10	20.1	20.7	1.8	9	20.3	0.5	2	−2.1
T_2-11	15.4	16.9	1.6	9	16.8	0.8	4	−0.1
T_2-12	10.9	12.2	2.6	21	12.2	0.6	5	−0.3

FIGURE 4 Comparison between SSE- and MESE-derived T_2 values for the NIST MnCl$_2$ phantom. The values were compared voxel-wise, for the nine different T_2 spheres, where each ROI included 47 voxels (ie, total number of voxels = 423). A, Correlation plot between MESE-based qT_2 values and SSE values ($R^2 = 0.996$); B, Bland-Altman plot of qT_2 difference versus mean T_2. The average difference between the two methods was found to be 1.6 ms ($p < 0.0001$), where the dashed lines represent ±1.96 SD from the mean difference, determining the limits of agreement as [−7.7, 10.9] ms. Higher T_2 difference and voxel disparity are observable for spheres with high T_2 values (ie spheres T_2-4 and T_2-5)

FIGURE 5 Reproducibility of T_2 values, measured on the NIST phantom for varying scan settings. Mean T_2 ± SD for each parameter set were measured for circular ROIs within each sphere. The average CV across the different scan settings and spheres was found to be 3%, affirming the high reproducibility of EMC-derived T_2 values. Scan parameters were the following: voxel resolution = 1.0 × 1.0, 1.6 × 1.6 mm^2; BW = 200, 300, 401 Hz/Px; slice thickness = 3, 4, 5 mm; N_{slices} = 1, 3, 5, 9, 11 (inter-slice gap = 0%); inter-slice gap = 0, 50, 100, 200% (N_{slices} = 5); TR = 2000, 3000, 4000 ms; refocusing FA = 180°, 160°, 140°
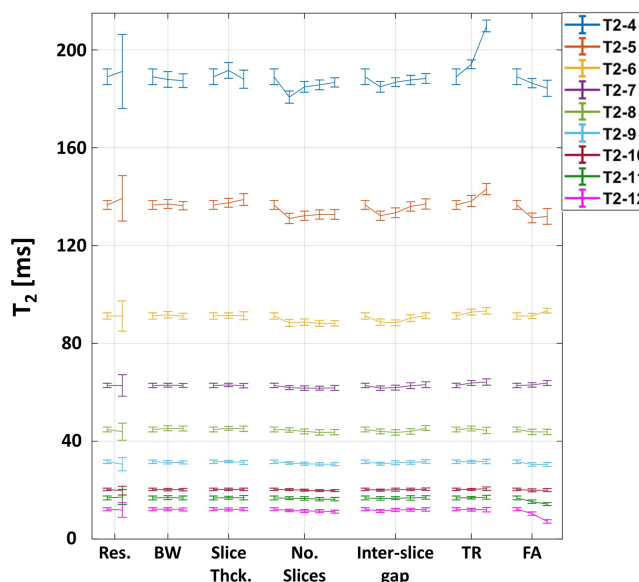
signify where most of the measurements are likely to be found. A linear correlation was observed between the T_2 differences and means, corresponding to the equation $T_{2,diff} = 0.06 \times T_{2,mean} - 2.31$ (blue dotted line, $R^2 = 0.694$), where underestimation of the SSE values appears for the long T_2 spheres, most likely due to diffusion effects.

Test-retest reliability was evaluated by repeating the same MESE scan 15 times. The mean $T_2 \pm$ SD values for each sphere were then measured, yielding an average intra-scanner variability (for all nine spheres) of 0.3 ± 0.3 ms and CV of $0.5 \pm 0.2\%$. These scores verify the high repeatability of the EMC-derived values. Remaining variations between the repetitive scans can be attributed to temperature variations, although no statistically significant trend was found between early and later protocol repetitions.

The NIST phantom was also used to measure the *reproducibility* of EMC-derived values (Figure 5). In this case, MESE scans were repeated for different scan settings, and the results were compared with the reference values in Table 1. T_2 values were evaluated across the different parameter sets and for each sphere, yielding the following mean $\pm$ SD [ms] (CV [%]) values: 188.6 ± 6.1 (3.2), 135.4 ± 3.4 (2.5), 90.6 ± 1.8 (1.9), 62.7 ± 0.8 (1.2), 44.4 ± 0.7 (1.5), 31.1 ± 0.5 (1.5), 20.1 ± 0.2 (1.2), 16.6 ± 0.7 (4.2), 11.5 ± 1.2 (10.2). The ROI segmentation and full set of results are available in Figure S4 and Tables S1-S7 in the supplementary materials.

For in vivo measurements, the raw data of both SSE and MESE were denoised. An example of an EMC-based T_2 map with and without denoising is illustrated in Figure 6. The denoising effect appears as a light smoothing in most of the brain tissues, while large variations appear in the CSF areas (ie in very long T_2 components, >1 s).

The EMC fitting in vivo accuracy and reproducibility are illustrated in Figures 7 and 8 for five healthy volunteers. The values were extracted from five brain ROIs (see the segmented ROIs in Figure S5) and were averaged across the volunteers to evaluate the inter-subject variability. Figure 7 shows the in vivo accuracy, measured between the SSE data, processed using exponential fitting, and MESE data, reconstructed using the EMC algorithm. Averaged across all brain regions and volunteers, the mean T_2 difference between the protocols was 0.8% (exhibiting both over- and underestimation of T_2 values), while the average absolute difference was 2.7%. These differences may result from motion during the long SSE scan and more prominent diffusion bias of the SSE data. For each volunteer, the CV was averaged across the brain ROIs, yielding an inter-scanner variability of 3.1% and 2.2% for SSE and MESE, respectively.

The in vivo reproducibility is presented in Figure 8, where the mean $\pm$ SD of T_2 values were calculated for different MESE scan settings. The average T_2 values across scan settings in all brain ROIs were the following: 31.8 ± 0.8 ms (parietal bone), 53.9 ± 1.5 ms (genu of CC), 57.3 ± 0.5 ms (WM fascicles), 66.5 ± 1.3 ms (thalamus), and 80.7 ± 1.5 ms (insular GM). Combining all ROIs, the inter-subject variability for different MESE scans was 3.2% (see the segmented ROIs in Figure S5).

3.3 | Effect of T_1 relaxation on qT$_2$ values

Figure 9 shows the simulated EMCs for a series of T_1 and T_2 value pairs. The values represent a physiological range of relaxation values and T_1/T_2 ratios at 3 T.[28-31] Figure 9A shows the EMCs of relatively short T_2 components of 15 and 20 ms, simulated with four T_1 values of 200, 300, 400, and 500 ms. Figure 9B illustrates longer T_2 values of 50 and 60 ms, simulated with T_1 values of 650, 1100, 1550, and 2000 ms. The resulting decay patterns are dominated by their T_2 values, with a negligible dependence on T_1, indicating the uniform effect that T_1 weighting has on the echo train. Practically, this means that a fixed value of T_1 can be used for the EMC dictionary generation (eg $T_1 = 1$ s for brain tissue), owing to the poor sensitivity of the decay curve to variations in T_1.
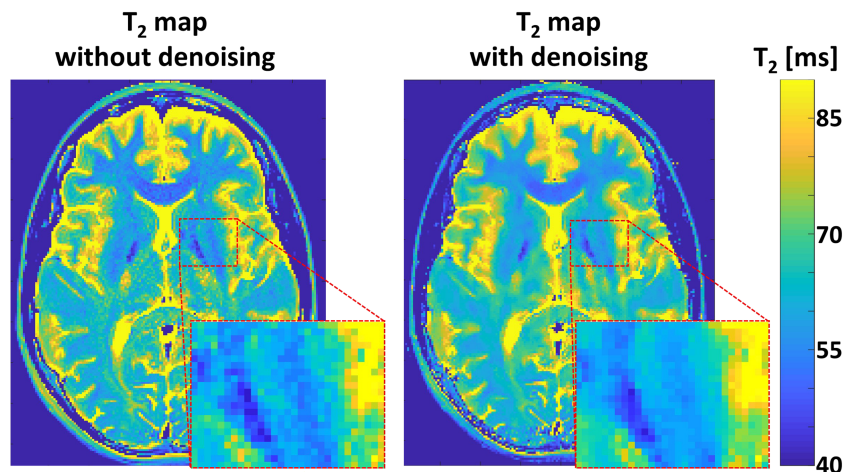

FIGURE 6 Example of the effectiveness of denoising EMC-based T_2 maps. The magnified insets include the area between the left globus pallidus and insular GM, and highlight the smoother texture of the denoised map without loss of morphological features
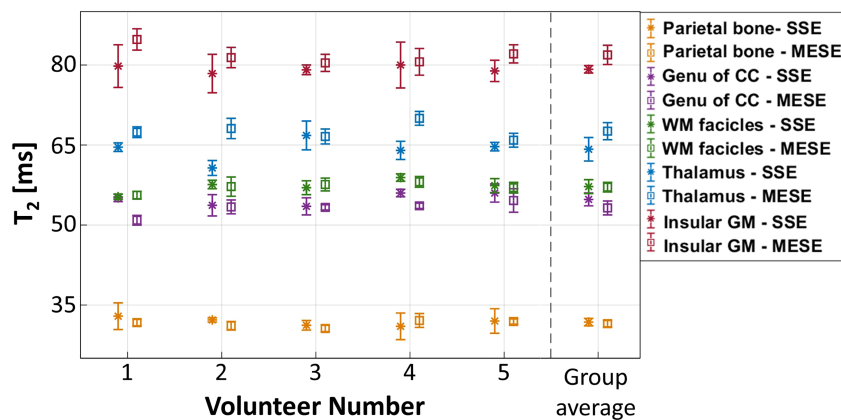
FIGURE 7 Accuracy of T_2 maps for five healthy volunteer brains. Mean ± SD of T_2 values were calculated in five brain ROIs (4 × 4 voxels each) using both SSE (exponential fitting, asterisks) and MESE (EMC fitting, squares) data. The selected ROIs represent a typical range of T_2 values of the brain tissue and are located at the parietal bone, genu of CC, frontal lobe WM fascicles, thalamus, and insular GM. T_2 values were also averaged across all five volunteers, and the mean ± SD are under "Group average" (see the segmented ROIs in Figure S5)
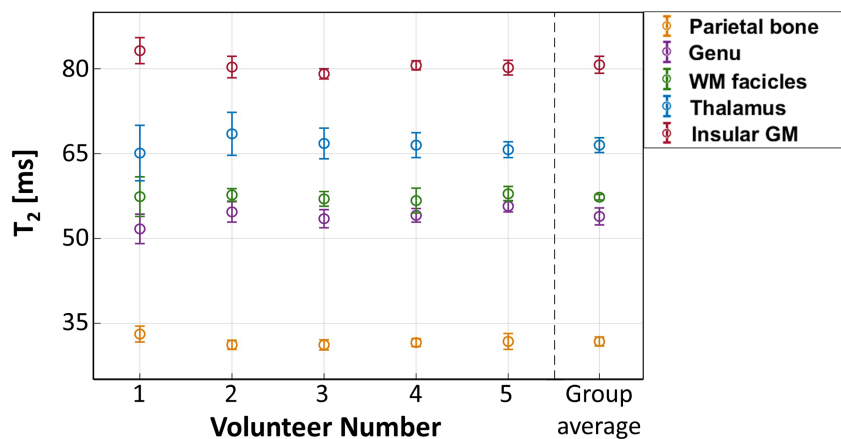

FIGURE 8 In vivo reproducibility measured on five healthy volunteer brains. Mean ± SD of T_2 values were extracted from MESE data, using five different scan settings. Values were calculated in five brain ROIs (4 × 4 voxels each), representing a typical range of brain T_2 values, and located in the parietal bone, genu of CC, WM fascicles, thalamus, and insular GM. T_2 values were also averaged across all five volunteers, and the mean ± SD are plotted under "Group average" (see the segmented ROIs in Figure S5). Error bars represent the SD of mean T_2 values across the five different scan settings
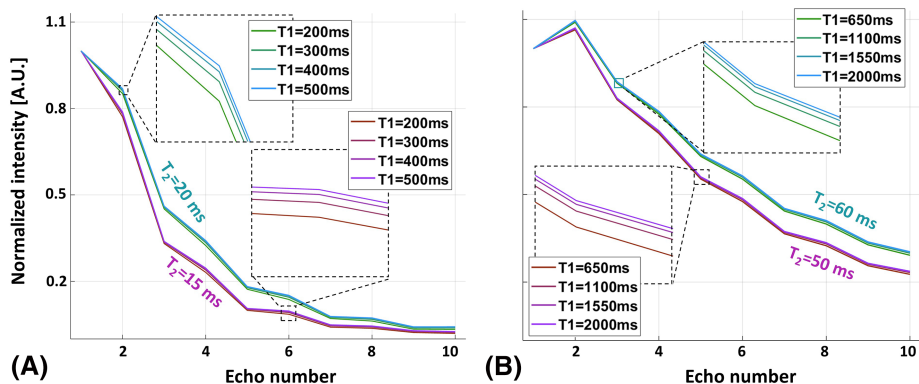

FIGURE 9 The effect of T_1 on EMC T_2 fitting. Sixteen EMCs were simulated for a range of physiological T_1/T_2 ratios, and divided into two plots: A, T_2 = 15 and 20 ms, with T_1 = 200:100:500 ms each, and B, T_2 = 50 and 60 ms, with T_1 = 650:450:2000 ms each. The echo spacing was set to 13 ms and ETL to 10. Assuming homogeneous B_0 and B_1^+ fields, the two batches vary according to the relaxation times solely, exhibiting high dependence on the T_2 value and negligible dependence on the T_1 value (see the magnified insets)

3.4 | Estimation of fat-water fraction

An extension of the EMC algorithm for fitting both fat and water T_2 components allowed us to reconstruct fat-water fraction maps of diseased thigh muscle. An example for a patient with genetically confirmed dysferlinopathy is shown in Figure 10 vis-à-vis a reference map generated using the three-point Dixon technique.[33] EMC-based values were in agreement with Dixon measurements, with an average score of 61.7% versus 58.3% for Biomarker 1 and 8.1 ± 12.3% versus 11.0 ± 10.6% for Biomarker 2 for the two techniques respectively. Another useful feature of the EMC platform is the ability to provide information regarding the T_2 value of the water component, yielding an average of 25.6 ± 3.8 ms in the viable muscle region, ie where the fat fraction is smaller than 50%. This additional information is useful for identifying biochemical changes to the tissue like early inflammatory processes.

4 | DISCUSSION

This work describes the EMC platform, used to quantify T_2 relaxation and PD maps from MESE data. The use of quantitative maps offers higher sensitivity to tissue changes, thereby allowing to investigate subclinical presentation of symptoms, and to identify the variation of disease biomarkers over time.[26] Notwithstanding their advantages, the integration of qMRI techniques in clinical settings is still hindered by the lack of standardization, and inter-/intra-scanner variability. Thus, routine clinical diagnosis is typically based on *qualitative* examination of contrast-weighted images, as in the case of MS, where disease progression is estimated based on lesion load[35]—an approach that lacks sensitivity to subtle tissue changes in normal-appearing tissues. Recent studies have tried to estimate the sensitivity of radiologists to MS-related lesions,[36] and in some cases to compare them with deep learning techniques.[37] Still, to the best of our knowledge, an explicit comparison between qMRI and common qualitative diagnosis has not been reported.

The EMC technique maps T_2 relaxation times. We note that relaxation times, in some cases, can be treated as complex numbers, particularly in inhomogeneous tissues such as the lungs,[14] where the real part describes the signal attenuations, and the imaginary part describes phase oscillations.[38] This interpretation is, for example, common with T_2^* and magnetic susceptibility mapping, where the phase images are used for background field removal and phase unwrapping.[39]

The EMC platform employs several strategies in order to produce accurate T_2 values. First, it uses full Bloch simulations to overcome signal biases due to stimulated echoes.[40,41] These render exponential fitting procedures (eg skipping echoes[15]) irrelevant and necessitate the use of more advanced signal models. When comparing Bloch simulations with EPG-based fitting for example, higher accuracy is achieved for the former, owing to more faithful simulation of the pulse sequence diagram, and in particular the ability to sample the excitation and refocusing RF profiles much more densely.[42] Second, it avoids bias attributed to Rician noise, particularly at short T_2 values or low SNR, by truncating the signal decay curve when it decreases below 10% of the first echo intensity. Another SNR improvement is achieved through a preprocessing denoising of the raw MESE images.[27] Third, it imposes spatial smoothness of the B_1^+ field. Finally, and most importantly, each fitting process is tailored to the particular pulse sequence timing diagram and parameter values, thereby offering both accuracy and reproducibility across scanners and scan settings.
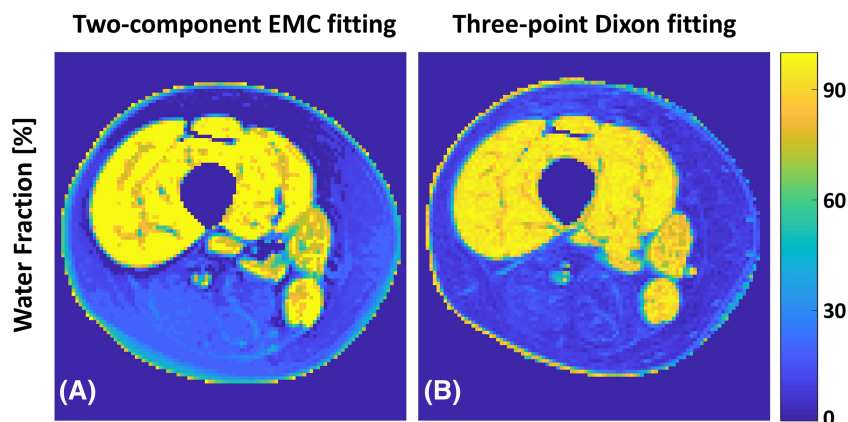

Two-component EMC fitting   **Three-point Dixon fitting**

Water Fraction [%]

(A)   (B)

FIGURE 10   Quantitative fat-water fraction maps of an axial slice of a thigh muscle from a patient with dysferlinopathy, demonstrating the infiltration of fat into the diseased muscle region. Healthy and diseased muscle segments were used to evaluate the performance of the EMC algorithm (A),[32] and the three-point DIXON technique (B).[33] Both maps were automatically segmented using a deep learning neural network to exclude the femur bone.[34] The two protocols did not cover the exact slice location due to patient motion between scans, accounting for the small anatomic differences between the two images

The methods' accuracy was evaluated on the NIST phantom[26] with respect to reference SSE T_2 values, showing an average relative difference of 0.4%, with higher error for long T_2 values due to the fact that their signal decay was not sufficiently sampled (ie significantly longer than the maximal sampled TE). The SD of the mean absolute error was 2.9%, reflecting the method's precision with respect to the reference values. The reproducibility of EMC qT_2 values was investigated, showing their stability across different scan settings, and even in the presence of MT. The validation experiments presented herein exhibit an average CV of 3% for all assayed T_2 values and across different spatial resolutions, acquisition BWs, slice thicknesses, number of slices, inter-slice gap, TR, and refocusing FAs.

The in vivo accuracy and reproducibility results were similar to the phantom results. For different scan settings, the in vivo T_2 values exhibited higher CVs than for phantom scans, possibly due to intra-voxel compartmentalization, partial-volume effect, and motion occurring between the repeated MESE scan. Additional in vivo validation of the reproducibility of EMC-derived values is available in Reference 40. In that case, the mean, SD, and CV of T_2 values were measured 24 times, using two scanners and six different scan settings, yielding an intra-subject CV of 2.5% (ie for different scanners and scan settings), an inter-scanner CV of 0.7% (ie same scan parameters on two different scanners), and an intra-scanner CV of 1.6% (ie same scanner with varying scan parameters).

The accuracy and precision of the T_2 maps depend on the underlying signal model, but also on the selected acquisition protocol and scan settings. While MESE is the most sensitive protocol when it comes to T_2 relaxation time, this sensitivity will depend on the chosen echo spacing and the maximal TE. For typical brain tissues, where the T_2 values of WM and GM range between 50 and 80 ms, an echo spacing of 10 ms and a maximal TE of 150 ms (ie, ETL = 15) will provide sufficient accuracy. For tissues with longer T_2 values, eg CSF where the T_2 is about 2 s, the maximal TE must be at least 1.7 times the T_2 value, dramatically increasing the total scan time, given that minimal TR = maximal $TE \times N_{slices}$. The optimal echo spacing and number of echoes should thus match the range of T_2 values in the target tissues.

4.1 | Effects of MT

The transfer of magnetization between free water pools, and fast relaxing macromolecular pools (MMPs) (ie, $T_2 < 1$ ms)[43] is a well known process affecting MR images. This contrast mechanism plays an important role in WM studies, quantifying the ratio of myelin versus the intra-/extra-cellular water pools.[13] MT is more prominent in MESE protocols due to the extensive use of RF pulses, which lead to significant off-resonance saturation of the MMP.[44] Specifically, MT interactions accumulate along the echo train, and "accelerate" the signal decay rate,[22] leading to underestimation of the measured T_2 values. The influence of MT varies for different tissues, depending on their MMP content (ie types of molecule, their concentrations, and exchange rates). Moreover, MT-related qT_2 bias depends on the RF duration and amplitude[45] as well as on the microstructural compartmentation.[13] The influence of MT on T_2 values can also be seen when using the mcDESPOT sequence, where the use of long RF pulses led to increased MT, resulting in underestimation of T_2 values compared with the use of short RF pulses.[46]

Factoring out MT effects is challenging to due to the coupling between MT-related and T_2-related decay, and the lack of MT-free qT_2-encoding protocol. One alleviating aspect is that the amount of MT saturation will be similar across multi slice MESE scan settings, resulting in minimal variability across scanners and experimental parameter values.

We further note that 3D MESE acquisitions suffer from significantly less MT- and stimulated-echo-related signal distortions, owing to the use of non-selective refocusing pulses. Such protocols, however, are much less practical compared with 2D multi-slice MESE, since the scan times are significantly longer.

4.2 | Clinical applicability

Several pulse sequences and advanced processing techniques have been developed to quantify T_2 values with high accuracy and reproducibility, aiming to reveal the clinical utility of this relaxation time. For example, Otto et al[47] used the EPG to observe upper leg involvement in spinal muscular atrophy, Yuan et al[48] used 3D Fast-SE to map the black-blood T_2, and Bouhrara et al[49] used mcDESPOT to explore demyelination in mild cognitive impairment and dementia.

The potential of the EMC platform in clinical practice was investigated on several anatomies and pathologies. Nassar et al[32] used the two-component EMC approach to investigate muscle dystrophies and neuromuscular disorders. One of the major symptoms is the abnormal accumulation of fat within muscle tissue. A voxel containing both fat and water will, in this case, exhibit an averaged contribution of two T_2 components. Being able to separate the two components has high clinical merit, both for improving early diagnosis, and for accurate follow-up of the disease progression. Thus, by incorporating multi-compartment analysis, algorithms such as the EMC can track the local water-fat fractions and serve as biomarkers of muscle state.[50]

Shepherd et al[40] studied the utility of EMC-based T_2 mapping to identify changes in different brain regions of relapsing-remitting MS (RRMS) patients. RRMS is a neurological disease, characterized by symptomatic episodes of inflammation and neurodegeneration, leading to progressive disability. Current clinical diagnosis relies mostly on changes in T_2-weighted images,[5,13] while early pathological changes induce only subtle

changes in T_2 values, which are hard to detect visually and require more sensitive techniques.[51] EMC-derived T_2 values were able to identify pathological changes in normal-appearing WM and GM structures, attesting to the potential of qT_2 for investigating this disease. Findings also included statistically significant T_2 changes within the WM of healthy controls, further emphasizing the sensitivity of this technique.

Ben-Eliezer et al[21] used the EMC platform to examine the T_2 values in the hip cartilage of femoroacetabular impingement (FAI) patients. FAI is characterized by bony abnormalities in the hip joint that can damage the acetabular cartilage (ACT) and labrum.[52] Early diagnosis can prevent the progression of cartilage degeneration and improve surgical outcome.[53] Previous reports have shown that biochemical changes, including cartilage hydration and collagen remodeling, can be detected using qT_2,[54] yet it is still challenging to set a specific quantitative threshold due to the intrinsic variability between patients and lesions. Assessment of the utility of T_2 values as a biomarker for biochemical changes, was based on a normalized T_2 index, calculated as the ratio between the T_2 value at the weight-bearing ACT area, and the T_2 value at the central region of the femoral part. This generated a reliable and patient-specific index, which avoids inter-subject variability, and does not depend on scan settings or and patient positioning, making it an effective self-referenced biomarker for cartilage damage.

Hoch et al[55] combined the EMC platform with neuronal track density imaging and simultaneous multi-section acquisition to reveal the brain stem anatomy. This approach can be useful in specific clinical cases where the internal anatomy needs to be probed with high resolution, eg for investigating progressive supranuclear palsy and multiple system atrophy.[56] The resulting overall scan time was 20 min in that case, divided into 6 min for the MESE scan and 14 min for the high-angular-resolution diffusion sequence, which limits routine clinical use.

4.3 | Outstanding challenges

MESE protocols are exposed to a wide range of influencing factors, including stimulated echoes, molecular diffusion, magnetization exchanges, and J-coupling.[57] While the EMC algorithm is based on Bloch simulations, and thereby overcomes stimulated echo bias, it does not incorporate some of the other abovementioned mechanisms, leading to a small bias in the measured T_2 values compared with SSE. Another limitation of multi-RF acquisition schemes is the high specific absorption rate deposition. This can be easily alleviated through the use of lower FA (eg 160°). Finally, EMC reconstruction is still done offline, requiring about 20 s for processing a set of 30 slices (acceleration of the postprocessing is based on principal component analysis compression of the data and the corresponding search dictionary). Incorporation of the fitting procedure on a scanner's console is thus needed in order to facilitate clinical use.

Finally, EMC fitting produces a single T_2 value at each voxel. This value is actually a spatiotemporal average over multiple T_2 components residing within the voxel (eg compartmentation in the WM[28]). Extending the platform to multi-component analysis (see, eg, References 58 and 59) can improve qMRI's ability to probe micro- and mesoscopic information, while also decreasing partial volume effects.

DATA AVAILABILITY STATEMENT

All data presented in this study will be available upon request.

REFERENCES

1. Marty B, Baudin P-Y, Reyngoudt H, et al. Simultaneous muscle water T_2 and fat fraction mapping using transverse relaxometry with stimulated echo compensation. *NMR Biomed*. 2016;29(4):431-443. https://doi.org/10.1002/nbm.3459
2. Noth U, Tichy J, Tritt S, Bahr O, Deichmann R, Hattingen E. Quantitative T1 mapping indicates tumor infiltration beyond the enhancing part of glioblastomas. *NMR Biomed*. 2020;33(3):1-11, e4242. https://doi.org/10.1002/nbm.4242
3. Uhrig M, Mueller J, Longerich T, et al. Susceptibility based multiparametric quantification of liver disease: non-invasive evaluation of steatosis and iron overload. *Magn Reson Imaging*. 2019;63:114-122. https://doi.org/10.1016/j.mri.2019.08.016
4. Siemonsen S, Mouridsen K, Holst B, et al. Quantitative T2 values predict time from symptom onset in acute stroke patients. *Stroke*. 2009;40(5):1612-1616. https://doi.org/10.1161/STROKEAHA.108.542548
5. Lund H, Jønsson A, Andresen J, Rostrup E, Paulson OB, Sørensen PS. Cognitive deficits in multiple sclerosis: correlations with T2 changes in normal appearing brain tissue. *Acta Neurol Scand*. 2012;125(5):338-344. https://doi.org/10.1111/j.1600-0404.2011.01574.x
6. Liu L, Yin B, Shek K, et al. Role of quantitative analysis of T2 relaxation time in differentiating benign from malignant breast lesions. *J Int Med Res*. 2018;46(5):1928-1935. https://doi.org/10.1177/0300060517721071
7. Kurz FT, Kampf T, Heiland S, et al. Theoretical model of the single spin-echo relaxation time for spherical magnetic perturbers. *Magn Reson Med*. 2014;71(5):1888-1895. https://doi.org/10.1002/mrm.25196
8. Virtanen JM, Komu ME, Parkkola RK. Quantitative liver iron measurement by magnetic resonance imaging: in vitro and in vivo assessment of the liver to muscle signal intensity and the R2* methods. *Magn Reson Imaging*. 2008;26(8):1175-1182. https://doi.org/10.1016/j.mri.2008.01.028
9. Burstein D. Stimulated echoes: description, applications, practical hints. *Concepts Magn Reson*. 1996;8(4):269-278. https://doi.org/10.1002/(SICI)1099-0534(1996)8:4%3C269::AID-CMR3%3E3.0.CO;2-X

10. Hennig J. Multiecho imaging sequences with low refocusing flip angles. *J Magn Reson*. 1988;78(3):397-407. https://doi.org/10.1016/0022-2364(88)90128-X

11. Poon CS, Henkelman RM. Practical T2 quantitation for clinical applications. *J Magn Reson Imaging*. 1992;2(5):541-553. https://doi.org/10.1002/jmri.1880020512

12. Sled JG, Pike GB. Correction for B_1 and B_0 variations in quantitative T_2 measurements using MRI. *Magn Reson Med*. 2000;43(4):589-593. https://doi.org/10.1002/(SICI)1522-2594(200004)43:4%3C589::AID-MRM14%3E3.0.CO;2-2

13. MacKay A, Laule C, Vavasour I, et al. Insights into brain microstructure from the T2 distribution. *Magn Reson Imaging*. 2006;24(4):515-525. https://doi.org/10.1016/J.MRI.2005.12.037

14. Mulkern R, Haker S, Mamata H, et al. Lung parenchymal signal intensity in MRI: a technical review with educational aspirations regarding reversible versus irreversible transverse relaxation effects in common pulse sequences. *Concepts Magn Reson A*. 2014;43A(2):29-53. https://doi.org/10.1002/cmr.a.21297

15. McPhee KC, Wilman AH. Limitations of skipping echoes for exponential T2 fitting. *J Magn Reson Imaging*. 2018;48(5):1432-1440. https://doi.org/10.1002/jmri.26052

16. Huang C, Bilgin A, Barr T, Altbach MI. T_2 relaxometry with indirect echo compensation from highly undersampled data. *Magn Reson Med*. 2013;70(4):1026-1037. https://doi.org/10.1002/mrm.24540

17. Lebel RM, Wilman AH. Transverse relaxometry with stimulated echo compensation. *Magn Reson Med*. 2010;64(4):1005-1014. https://doi.org/10.1002/mrm.22487

18. Ehses P, Seiberlich N, Ma D, et al. IR TrueFISP with a golden-ratio-based radial readout: fast quantification of T_1, T_2, and proton density. *Magn Reson Med*. 2013;69(1):71-81. https://doi.org/10.1002/mrm.24225

19. Deoni SCL, Peters TM, Rutt BK. High-resolution T_1 and T_2 mapping of the brain in a clinically acceptable time with DESPOT1 and DESPOT2. *Magn Reson Med*. 2005;53(1):237-241. https://doi.org/10.1002/mrm.20314

20. Ben-Eliezer N, Sodickson DK, Block TK. Rapid and accurate T_2 mapping from multi spin echo data using Bloch-simulation-based reconstruction. *Magn Reson Med*. 2015;73(2):809-817. https://doi.org/10.1002/mrm.25156

21. Ben-Eliezer N, Raya JG, Babb JS, Youm T, Sodickson DK, Lattanzi R. A new method for cartilage evaluation in femoroacetabular impingement using quantitative T2 magnetic resonance imaging: preliminary validation against arthroscopic findings. *Cartilage*. 2019:1-9. https://doi.org/10.1177/1947603519870852

22. Radunsky D, Blumenfeld-Katzir T, Volovyk O, et al. Analysis of magnetization transfer (MT) influence on quantitative mapping of T_2 relaxation time. *Magn Reson Med*. 2019;82(1):145-158. https://doi.org/10.1002/mrm.27704

23. Bnaiahu N, Wilczynski E, Levy S, Omer N, Blumenfeld-Katzir T, Ben-Eliezer N. Compensating diffusion bias of quantitative T2 mapping on high-field MRI scanners. In *Proceedings of the 28th Annual meeting of ISMRM, Montreal, Canada*. 2019:5437. https://archive.ismrm.org/2020/3415.html

24. Gudbjartsson H, Patz S. The Rician distribution of noisy MRI data. *Magn Reson Med*. 1995;34(6):910-914. https://doi.org/10.1002/mrm.1910340618

25. Lin L, Sherman PD. In *Proceedings of the SouthEast SAS Users Group, Hilton Head Island, SC, USA*, 2007. SESUG Proceedings, Paper SA11. https://www.nbi.dk/~petersen/Teaching/Stat2017/Notes/StatNote_RejectingData.pdf

26. Keenan KE, Biller JR, Delfino JG, et al. Recommendations towards standards for quantitative MRI (qMRI) and outstanding needs. *J Magn Reson Imaging*. 2019;49(7):e26-e39. https://doi.org/10.1002/jmri.26598

27. Does MD, Olesen JL, Harkins KD, et al. Evaluation of principal component analysis image denoising on multi-exponential MRI relaxometry. *Magn Reson Med*. 2019;81(6):3503-3514. https://doi.org/10.1002/mrm.27658

28. Vavasour IM, Whittall KP, Li DK, MacKay AL. Different magnetization transfer effects exhibited by the short and long T_2 components in human brain. *Magn Reson Med*. 2000;44(6):860-866. https://doi.org/10.1002/1522-2594(200012)44:6%3C860::AID-MRM6%3E3.0.CO;2-C

29. Oh J, Han ET, Pelletier D, Nelson SJ. Measurement of in vivo multi-component T2 relaxation times for brain tissue using multi-slice T2 prep at 1.5 and 3 T. *Magn Reson Imaging*. 2006;24(1):33-43. https://doi.org/10.1016/j.mri.2005.10.016

30. Bojorquez JZ, Bricq S, Acquitter C, Brunotte F, Walker PM, Lalande A. What are normal relaxation times of tissues at 3 T? *Magn Reson Imaging*. 2017;35:69-80. https://doi.org/10.1016/j.mri.2016.08.021

31. Du J, Sheth V, He Q, et al. Measurement of T1 of the ultrashort T2* components in white matter of the brain at 3T. *PLoS ONE*. 2014;9(8):1-8, e103296. https://doi.org/10.1371/journal.pone.0103296

32. Nassar J, Le Fur Y, Radunsky D, Blumenfeld-Katzir T, Bendahan D, Ben-Eliezer N. Sub-voxel estimation of fat infiltration in degenerative muscle disorders using multi-T2 analysis—a quantitative disease biomarker. In *Proceedings of the 28th Annual Meeting of ISMRM, Montreal, Canada*. 2019:4011. http://archive.ismrm.org/2019/4011.html

33. Glover GH, Schneider E. Three-point Dixon technique for true water/fat decomposition with B_0 inhomogeneity correction. *Magn Reson Med*. 1991;18(2):371-383. https://doi.org/10.1002/mrm.1910180211

34. Amer R, Nassar J, Bendahan D, Greenspan H, Ben-Eliezer N. Automatic segmentation of muscle tissue and inter-muscular fat in thigh and calf MRI images. *Lect Notes Comput Sci*. 2019;11765:219-227. https://doi.org/10.1007/978-3-030-32245-8_25

35. Filippi M, Rocca MA, Ciccarelli O, et al. MRI criteria for the diagnosis of multiple sclerosis: MAGNIMS consensus guidelines. *Lancet Neurol*. 2016;15(3):292-303. https://doi.org/10.1016/S1474-4422(15)00393-2

36. Woo JH, Henry LP, Krejza J, Melhem ER. Detection of simulated multiple sclerosis lesions on T2-weighted and FLAIR images of the brain: observer performance. *Radiology*. 2006;241(1):206-212. https://doi.org/10.1148/radiol.2411050792

37. Liu X, Faes L, Kale AU, et al. A comparison of deep learning performance against health-care professionals in detecting diseases from medical imaging: a systematic review and meta-analysis. *Lancet Digit Health*. 2019;1(6):e271-e297. https://doi.org/10.1016/S2589-7500(19)30123-2

38. Ziener CH, Uhrig M, Kampf T, et al. Lineshape of magnetic resonance and its effects on free induction decay and steady-state free precession signal formation. *Concepts Magn Reson A*. 2020;2020:1-17, 5057386. https://doi.org/10.1155/2020/5057386

39. Chen Z, Calhoun V. Intrinsic functional brain mapping in reconstructed 4D magnetic susceptibility (χ) data space. *J Neurosci Methods*. 2015;241:85-93. https://doi.org/10.1016/j.jneumeth.2014.12.014

40. Shepherd TM, Kirov II, Charlson E, et al. New rapid, accurate T2 quantification detects pathology in normal-appearing brain regions of relapsing-remitting MS patients. *NeuroImage Clin*. 2017;14:363-370. https://doi.org/10.1016/j.nicl.2017.01.029

41. Ben-Eliezer N, Sodickson DK, Shepherd T, Wiggins GC, Block KT. Accelerated and motion-robust in vivo T_2 mapping from radially undersampled data using Bloch-simulation-based iterative reconstruction. *Magn Reson Med*. 2016;75(3):1346-1354. https://doi.org/10.1002/mrm.25558

42. McPhee KC, Wilman AH. Transverse relaxation and flip angle mapping: evaluation of simultaneous and independent methods using multiple spin echoes. *Magn Reson Med*. 2017;77(5):2057-2065. https://doi.org/10.1002/mrm.26285

43. Henkelman RM, Stanisz GJ, Graham SJ. Magnetization transfer in MRI: a review. *NMR Biomed*. 2001;14(2):57-64. https://doi.org/10.1002/nbm.683

44. Harrison R, Bronskill MJ, Henkelman RM. Magnetization transfer and T_2 relaxation components in tissue. *Magn Reson Med*. 1995;33(4):490-496. https://doi.org/10.1002/mrm.1910330406

45. Deoni SCL, Rutt BK, Peters TM. Rapid combined T_1 and T_2 mapping using gradient recalled acquisition in the steady state. *Magn Reson Med*. 2003;49 (3):515-526. https://doi.org/10.1002/mrm.10407

46. Zhang J, Kolind SH, Laule C, MacKay AL. How does magnetization transfer influence mcDESPOT results? *Magn Reson Med*. 2015;74(5):1327-1335. https://doi.org/10.1002/mrm.25520

47. Otto LAM, van der Pol WL, Schlaffke L, et al. Quantitative MRI of skeletal muscle in a cross-sectional cohort of patients with spinal muscular atrophy types 2 and 3. *NMR Biomed*. 2020;33(10):1-13, e4357. https://doi.org/10.1002/nbm.4357

48. Yuan J, Usman A, Reid SA, et al. Three-dimensional black-blood T_2 mapping with compressed sensing and data-driven parallel imaging in the carotid artery. *Magn Reson Imaging*. 2017;37:62-69. https://doi.org/10.1016/j.mri.2016.11.014

49. Bouhrara M, Reiter DA, Bergeron CM, et al. Evidence of demyelination in mild cognitive impairment and dementia using a direct and specific magnetic resonance imaging measure of myelin content. *Alzheimer's Dement*. 2018;14(8):998-1004. https://doi.org/10.1016/j.jalz.2018.03.007

50. Gloor M, Fasler S, Fischmann A, et al. Quantification of fat infiltration in oculopharyngeal muscular dystrophy: comparison of three MR imaging methods. *J Magn Reson Imaging*. 2011;33(1):203-210. https://doi.org/10.1002/jmri.22431

51. Bonnier G, Roche A, Romascano D, et al. Advanced MRI unravels the nature of tissue alterations in early multiple sclerosis. *Ann Clin Transl Neurol*. 2014;1(6):423-432. https://doi.org/10.1002/acn3.68

52. Beck M, Kalhor M, Leunig M, Ganz R. Hip morphology influences the pattern of damage to the acetabular cartilage. Femoroacetabular impingement as a cause of early osteoarthritis of the hip. *J Bone Jt Surg B*. 2005;87(7):1012-1018. https://doi.org/10.1302/0301-620X.87B7.15203

53. Beck M, Leunig M, Parvizi J, Boutier V, Wyss D, Ganz R. Anterior femoroacetabular impingement: Part II. Midterm results of surgical treatment. *Clin Orthop Relat Res*. 2004;418:67-73. https://doi.org/10.1097/00003086-200401000-00012

54. Mosher TJ, Dardzinski BJ. Cartilage MRI T2 relaxation time mapping: overview and applications. *Semin Musculoskelet Radiol*. 2004;8(4):355-368. https://doi.org/10.1055/s-2004-861764

55. Hoch MJ, Chung S, Ben-Eliezer N, Bruno MT, Fatterpekar GM, Shepherd TM. New clinically feasible 3T MRI protocol to discriminate internal brain stem anatomy. *Am J Neuroradiol*. 2016;37(6):1058-1065. https://doi.org/10.3174/ajnr.A4685

56. Rolland Y, Vérin M, Payan CA, et al. A new MRI rating scale for progressive supranuclear palsy and multiple system atrophy: validity and reliability. *J Neurol Neurosurg Psychiatry*. 2011;82(9):1025-1032. https://doi.org/10.1136/jnnp.2010.214890

57. Constable RT, Anderson AW, Zhong J, Gore JC. Factors influencing contrast in fast spin-echo MR imaging. *Magn Reson Imaging*. 1992;10(4):497-511. https://doi.org/10.1016/0730-725X(92)90001-G

58. Omer N, Galun M, Stern N, Blumenfeld-Katzir T, Ben-Eliezer N. A novel multicomponent T2 analysis for identification of sub-voxel compartments and quantification of myelin water fraction. In *Proceedings of the 29th Annual Meeting of ISMRM*, virtual meeting. 2020:1429. https://cds.ismrm.org/protected/20MPresentations/abstracts/1429.html

59. Akhondi-Asl A, Afacan O, Mulkern RV, Warfield SK. T_2-relaxometry for myelin water fraction extraction using Wald distribution and extended phase graph. In: Golland P, Hata N, Barillot C, Hornegger J, Howe R, eds. *Int Conf Med Image Comput*. Cham, Switzerland: Springer; 2014:145-152.

SUPPORTING INFORMATION

Additional supporting information may be found online in the Supporting Information section at the end of this article.